CHEMISTRY OF MATERIALS

pubs.acs.org/cm

Article

# Mechanisms of Electronic and Ionic Transport during Mg Intercalation in Mg−S Cathode Materials and Their Decomposition Products

Smobin Vincent, Jin Hyun Chang, Pieremanuele Canepa,* and Juan Maria García-Lastra*

Cite This: https://doi.org/10.1021/acs.chemmater.2c03784

Read Online

ACCESS | Metrics & More | Article Recommendations | Supporting Information

**ABSTRACT:** Rechargeable Mg−S batteries are attractive for next-generation energy storage devices due to their high theoretical energy density (1684 W h $kg^{-1}$ and 3286 W h $L^{-1}$) and low costs. The poor cycling performance of Mg−S batteries is linked to the formation of the solid discharge products, i.e., $MgS_2$ and MgS, which are electronic and ionic insulators. However, the formation of MgS itself contradicts such a premise because it requires further oxidation of $MgS_2$. Indeed, the insulating nature of $MgS_2$ should inhibit such an oxidation process in the first place. Using first-principles calculations and *ab initio* molecular dynamics simulations, we evaluate the charge transport associated with point defects in $MgS_2$ and MgS. In $MgS_2$, the single-electron polaron is the most abundant type of defect that emerges from our model, which appears at a low concentration at thermodynamic equilibrium but displays high mobility. However, under conditions far from thermodynamic equilibrium, mimicking those for battery operations, the concentration of electron polarons increases, enhancing the electronic conductivity in $MgS_2$. We demonstrate that in regimes far from thermodynamic equilibrium, the single-electron polarons coalesce to form double-electron polarons, whose mobilities are similar to that of a single-electron polaron. $MgS_2$ holds electronic conduction through a polaron migration mechanism for $\lesssim 3\,\mu m$ thick deposits, enabling further oxidation to form MgS. For MgS, our model suggests that the doubly positive Mg interstitial and doubly negative Mg vacancy are identified as the prevalent defects with high concentrations. However, due to the low mobility of these defects, their contribution to charge transport is negligible, which stops the oxidation process and severely hinders battery cyclability. Our results indicate that rechargeable Mg−S batteries can be developed if we ensure that the battery discharge does not push the oxidation process beyond the formation of $MgS_2$.

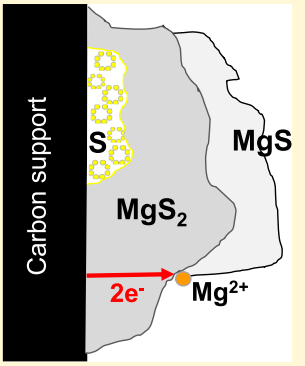


## INTRODUCTION

Rechargeable metal−sulfur batteries, such as Li−S, Mg−S, Ca−S, and Al−S batteries, are attracting significant interest as potential next-generation batteries due to their low cost and environmental sustainability and the abundance of sulfur.[1−4] In addition, metal−sulfur batteries offer high theoretical energy densities because of their use of metal as the anode material and high-gravimetric capacity sulfur as the positive electrode. Li−S (2654 W h $kg^{-1}$ and 2856 W h $L^{-1}$) and Mg−S (1684 W h $kg^{-1}$ and 3286 W h $L^{-1}$) batteries have the highest theoretical energy densities among the most studied metal−sulfur batteries.[1,5] In addition to their abundance and marginal costs,[1,6,7] Mg−S batteries possess an obvious advantage over their Li counterparts; namely, the dendrite-free nature of Mg reversible deposition at low current densities makes it a safer alternative,[8,9] which has attracted a great deal of attention as one of the next-generation battery technologies.

Despite the promise of Mg−S batteries, they pose a number of technical challenges that must be overcome before these batteries can be used in practical applications. One of the significant challenges is the poor cyclability of the sulfur cathode, where the magnesiation process during discharge is not highly reversible. Specifically, $Mg^{2+}$ ions are released from the Mg metal anode toward the sulfur cathode during discharge, forming various high-order polysulfides such as $MgS_8$, $MgS_6$, and $MgS_4$ (Figure 1a,b). The formation of these high-order polysulfide intermediates occurs at a higher rate due to their significant solubility in the electrolytes [e.g., $(HMDS)_2$ Mg-2 $AlCl_3$ in glymes[10] and MBA-$AlCl_3$ in THF[11]]. However, Gao et al.[12] showed that the kinetics of further reactions promoting the formation of shorter (poly)sulfide chains, i.e., $MgS_2$, become slower as they start to precipitate at the sulfur cathode in the form of $MgS_2$ (Figure 1c). A further reduction process occurs, in which $MgS_2$ partially becomes MgS (Figure 1d). Both precipitates, MgS and $MgS_2$, exhibit low $Mg^{2+}$ diffusivity and are insulating materials. This leads to a large overpotential at the trailing end of the charging process, as well as limited reversibility to high-order polysulfides and sulfur during charge.[13] At this point, a question arises. If $MgS_2$ is an

Received: December 22, 2022
Revised: April 3, 2023

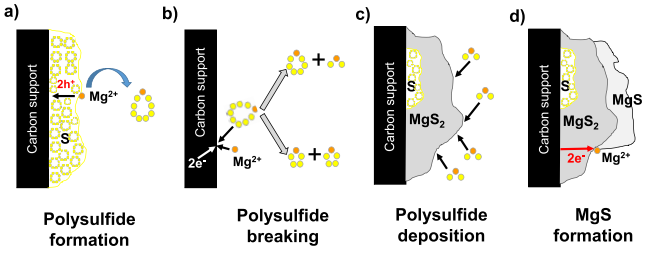


**Figure 1.** Different discharge stages at the positive electrode on the Mg−S battery. (a) Long polysulfides ($MgS_8$) are formed by combining reduced $S_8^{2-}$ rings with $Mg^{2+}$ ions in the electrolyte. Conduction of holes in $\alpha$-S is the source of charge for the redox process. (b) The long polysulfides break into shorter molecules. The electrochemical reaction most likely occurs by combining the $MgS_8$ rings with $Mg^{2+}$ ions from the electrolyte and electrons furnished by the carbon support. (c) The very short polysulfides ($MgS_2$) precipitate on the carbon support and unreacted $\alpha$-S. (d) $Mg^{2+}$ ions from the electrolyte react with the $MgS_2$ surface to form a MgS deposit. The conduction of electron polarons in $MgS_2$ provides the charge for the redox process.

insulating material, how is it possible that it is further reduced into MgS? Another follow-up arises. Is the formation of $MgS_2$ as detrimental with respect to battery cyclability as the formation of MgS? Understanding the charge transport properties in MgS and $MgS_2$ is crucial for answering these questions and will help in designing a functioning Mg−S battery with a long cycle life.

At present, the mechanism of charge transport in MgS and $MgS_2$ is not fully understood. Although few experimental and computational studies exist for MgS, the study of charge transport in $MgS_2$ remains unexplored. Most of the existing experimental studies of charge transport in MgS have been performed at an increased temperature (900 K),[14,15] whereas the conductivity at room temperature is certainly more important for battery applications. Presumably, the lack of an electrical conductivity measurement of MgS around room temperature stems from the difficulties in determining its low electrical conductivity due to its insulating nature. Several computational works also investigated charge transport in MgS. Using empirical interatomic potentials, Puntambekar et al. quantified the migration energies of $Mg^{2+}$ (~2.6 eV) and $S^{2-}$ (~3.4 eV) ions in MgS.[16] Using density functional theory (DFT), Chen et al. calculated a migration barrier of ~1.2 eV for $Mg^{2+}$ in MgS.[17] These studies mainly focused on ion transport, and little effort was devoted to studying electronic transport.

Using first-principles DFT calculations at the hybrid functional level of theory, we elucidate the charge transport mechanism in MgS and $MgS_2$. We study the ionic and electronic conductivity arising from the migration of charged point defects and polaronic defects (electron and hole polarons), respectively. The formation energies and the equilibrium concentrations of several point defects and polarons are calculated to identify the predominant defects. We evaluated the migration barrier for the prevalent defects. The calculated energy barrier is then used to estimate the maximum thickness of MgS and $MgS_2$ layers to achieve practical discharge rates. The transport mechanism under non-equilibrium conditions encompassing the injection (or extraction) of polarons and $Mg^{2+}$ from the positive electrode material is also investigated using *ab initio* molecular dynamics (AIMD).

Our study reveals that $MgS_2$ can achieve electronic conduction in the form of double electron polarons beyond 3 $\mu$m under practical battery operational conditions (typically at discharge rates of 1 C). This conduction mechanism enables further reduction and eventually the formation of MgS. In contrast, we demonstrate that MgS cannot hold any type of practical electronic or ionic conductivity. Our study highlights the importance of preventing the further oxidation of $MgS_2$ to MgS, encouraging the design of experimental strategies that can mitigate this undesired electrochemical process.

## METHODOLOGY

**Computational Details.** Spin-polarized first-principles calculations within the DFT approximation were performed using the Vienna Ab initio Simulation Package (VASP).[18,19] The commonly used PBE functional[20] is known to severely underestimate the bandgaps of semiconductors and insulators as well as not predicting the charge localization reliably (i.e., the charges are often delocalized).[21] Therefore, to predict the formation energies and migration barriers of defects, we used the Heyd−Scuseria−Ernzerhof (HSE06) screened hybrid functional.[22,23] Forty percent of the exact Hartree−Fock exchange was set to reproduce accurately the bandgap values from accurate GW-level calculations.[24−26] The wave functions were expanded in terms of plane waves with a kinetic energy cutoff of 520 eV. The projector-augmented wave (PAW) method was used to account for the core−valence interactions.[27] The convergence of electronic minimization was set to $10^{-6}$ eV. The atomic positions were relaxed until the stress on the cell and forces acting on each atoms fell below $10^{-2}$ eV Å$^{-1}$.

The predictions of the bandgap and dielectric constant of MgS and $MgS_2$ were based on the primitive unit cells. The sumo software package was used to plot the band structures and density of states of selected models.[28] The primitive unit cells of Mg, MgS, $MgS_2$, and S are used for the calculation of chemical potentials. For these systems, the first Brillouin zone was sampled with a dense Γ-centered $k$-point mesh with a minimum $k$-point density of 4 Å$^{-1}$. The calculations of the defect and mobility of the prevalent defects were carried out using a 2 × 2 × 2 supercell of the conventional cell, and the total energy was integrated at the Γ point.

**Formation Energy of Native Defects.** The likelihood of the defect formation was evaluated using the formation energy ($E_f$) of defect X. The $E_f$ of X with charge $q$ ($X^q$) was estimated according to

$$E_f(X^q) = E(X^q) - E_0 - \sum n_i\mu_i + q\varepsilon_f + E_{FNV} \quad (1)$$

where $E_0$ and $E(X^q)$ are the total energies of the pristine cell and the cell containing a point defect with charge $q$, respectively. $n_i$ is the number of atoms of species i removed while creating the defect. The value of $n_i$ becomes positive (negative) when a species is added to (removed from) the cell during the defect creation. $\mu_i$ denotes the chemical potential of species i and is determined directly from the phases that are in direct thermodynamic equilibrium with the material at 0 K. $\varepsilon_f$ is the Fermi energy referenced to the valence band maximum, and $E_{FNV}$ is the Freysoldt−Neugebauer−Vanderwall (FNV) correction for charged systems.[29] The FNV correction requires a dielectric constant of the material investigated, which was calculated using a self-consistent response of the material to a finite electric field.

The Python Charge Defects Toolkit (PYCDT) package[30] was used to generate the input structures and VASP setting files for the point defect calculations. The input structures of the polaron models were prepared manually by distorting the local geometry of the region where polaron localization is anticipated.

The concentration of defects, $c(X^q)$, was calculated using

$$c(X^q) = N \exp\left(\frac{-E_f}{k_B T}\right) \quad (2)$$


https://doi.org/10.1021/acs.chemmater.2c03784
Chem. Mater. XXXX, XXX, XXX−XXX

where $N$ is the number of equivalent sites of the defects, $k_B$ is the Boltzmann constant, and $T$ is the temperature. The ionic mobility of the defect ($M$) was calculated using the transition state theory:

$$M = \frac{\nu q a^2}{k_B T} \exp\left(\frac{-E_b}{k_B T}\right) \quad (3)$$

where $\nu$ is the frequency of the hopping, $a$ is the hopping distance, and $E_b$ is the migration barrier. The attempt frequency ($\nu$) was taken as $10^{13}$ s$^{-1}$ for both S and Mg.[31] The hopping distance ($a$) is the distance between the initial and final locations of the defects taken from the relaxed structures obtained via DFT. The migration barrier is predicted using the nudged elastic band (NEB)[32] method, as implemented in the atomic simulation environment (ASE) package.[33] The equilibrium conductivity of the defects ($\sigma$) was derived from $c(X^q)$ and $M$ as

$$\sigma = qc(X^q)M \quad (4)$$

The maximum diffusion length of a migrating defect (e.g., vacancy, interstitial, polaron, etc.) ($L$) is calculated using

$$L = \sqrt{Dt} \quad (5)$$

where $D$ is the diffusion coefficient ($D = Mk_BT/q$) and $t$ is the time for charging or discharging of the battery.

***Ab Initio* Molecular Dynamics.** The dynamics of the low-energy barrier defects under non-equilibrium conditions were evaluated using AIMD simulations. The molecular dynamics (MD) calculations were performed in a canonical ensemble ($NVT$) at 350 K, which was maintained by a Langevin thermostat as implemented in ASE with a friction coefficient of 0.05 atomic unit. The MD simulations used the same VASP settings but with adoption of the semilocal PBE functional to make the MD calculations possible. A preliminary step of equilibration of 0.5 ps was used for all cases, unless it is explicitly mentioned otherwise.

## RESULTS AND DISCUSSION

**Crystal Structure and Bandgaps.** The crystal structures of MgS and $MgS_2$ are illustrated in Figure S1. MgS exists as a rock-salt crystal structure (space group $Fm\bar{3}m$), where the $Mg^{2+}$ cations are octahedrally coordinated by $S^{2-}$ anions. The cubic pyrite structure (space group $Pa\bar{3}$) is reported to be the most stable structure for $MgS_2$,[34] which is a modified rock-salt structure in which the $S^{2-}$ anions of the rock-salt MgS are replaced by $S_2^{2-}$ dianions (S dimer). The calculated lattice constant $a$ for MgS, using HSE06, is ~5.17 Å, in excellent agreement with the experimental value of 5.17 Å.[35] The calculated lattice constant for $MgS_2$ using HSE06 is 6.07 Å. There is no experimentally measured value of $MgS_2$ to the best of our knowledge.

We computed the fundamental bandgaps of MgS and $MgS_2$ at three different levels of theory: $G_0W_0$, $GW_0$, and hybrid functional DFT HSE06. Wave functions generated with the PBE functional are used as the starting point for the $G_0W_0$ and $GW_0$ calculations using the structures (atom coordinates, shape, and volume) obtained from HSE06 calculations. The $GW_0$ approach yielded bandgaps of ~4.52 eV for MgS and ~4.33 eV for $MgS_2$, whereas the $G_0W_0$ approach yielded lower values of ~4.29 and ~3.88 eV for MgS and $MgS_2$, respectively. Previously, Shishkin and Kresse noted that the $GW_0$ approach best describes the bandgaps of semiconductors and insulators.[26] Thus, we take the bandgaps calculated using the $GW_0$ approach as a baseline to calibrate the amount of Hartree–Fock exchange in the definition of the HSE06 functional from its original value of $\alpha$ =0.25 to $\alpha$ =0.4, reproducing adequately the $GW_0$ bandgaps (Figure S2). The bandgaps obtained from the HSE06 ($\alpha$ = 0.4) calculation are ~4.49 and ~4.34 eV for MgS and $MgS_2$, respectively. The calculations using all three methods exhibit indirect bandgaps for both MgS and $MgS_2$. The band structures of MgS and $MgS_2$ are shown in Figure S3. Our results agree with those of previous theoretical studies employing hybrid functionals,[36,37] reporting an indirect bandgap in the range of approximately 4.0–4.8 eV for MgS.

**Localization of Polarons in MgS and $MgS_2$.** A polaron is formed when a localized charge (electron or hole) induces the polarization of the surrounding environment in the crystal, causing a lattice distortion in the vicinity of localized charge. Here, we aimed to localize four types of polarons: (i) a single-hole polaron ($h^\bullet$), (ii) a double-hole polaron ($h^{\bullet\bullet}$), (iii) a single-electron polaron ($e'$), and (iv) a double-electron polaron ($e''$).

In MgS, we successfully localized the $h^{\bullet\bullet}$ polaron. The sulfur atom in MgS has an oxidation state of −2. The removal of two electrons from MgS should, in principle, change the oxidation states of two adjacent sulfur atoms from −2 to −1. These S ions bearing a reduced formal charge experience weaker electrostatic repulsion, resulting in the formation of an S dimer as shown in Figure 2a. The formation of the $h^{\bullet\bullet}$ polaron

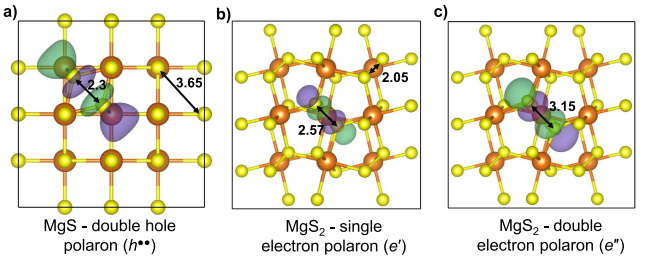


**Figure 2.** Γ point frontier orbitals of (a) $h^{\bullet\bullet}$ localized in MgS, (b) $e'$ localized in $MgS_2$, and (c) $e''$ localized in $MgS_2$. Numbers in each panel show the S–S distances in angstroms. Isosurfaces indicate the unoccupied $\sigma^*$ orbital in panel a) and occupied $\sigma^*$ orbitals in panels b) and c). The details regarding the bond length and occupation of the orbitals for these three cases are shown in Figure S4.

decreases the interatomic distance between the two S atoms from ~3.65 to ~2.3 Å. The necessary condition to form the $h^{\bullet\bullet}$ polaron requires an initial local geometry indicating that one of the S–S bonds in the structure is shortened. The absence of such an initial distortion drives the delocalization deviating from the localization of a polaron. The localization of $h^{\bullet\bullet}$is also evident from the plot of the density of states (DOS) in Figure S5. The delocalization energy (i.e., the difference in total energy between the structures with delocalized and localized charges) for $h^{\bullet\bullet}$ in MgS is calculated to be approximately −0.21 eV. A negative delocalization energy indicates that it is thermodynamically favored to have $h^{\bullet\bullet}$ in the system than to have delocalized charges. A previous study of MgO, which has a rock-salt structure similar to that of MgS, demonstrated that $h^\bullet$ is formed in that material.[38] Although a $h^\bullet$ could be localized on a single O atom in MgO,[38] we were not able to obtain a stable structure for the single-hole polaron in the sulfur analogues (MgS).

For $MgS_2$, we were able to localize $e'$ and $e''$. Unlike the formation of $h^{\bullet\bullet}$ in MgS, the excess electron introduced into the cell forms $e'$ spontaneously without any initial structural distortion of the lattice. This points out the stability of this defect. On one hand, Figure 2b shows the localization of $e'$ on an S dimer, which causes an increase in the S–S bond distance from ~2.05 to ~2.57 Å. On the other hand, the formation of


https://doi.org/10.1021/acs.chemmater.2c03784
Chem. Mater. XXXX, XXX, XXX–XXX

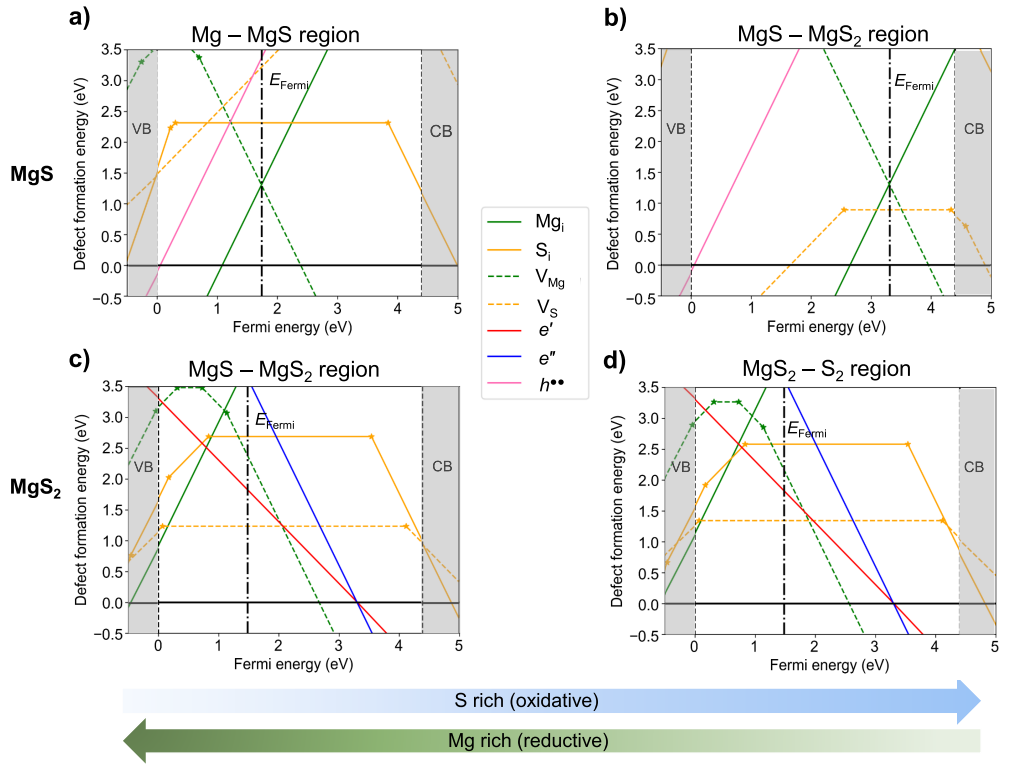


**Figure 3.** Predicted defect formation energies in MgS and $MgS_2$. The equilibrium Fermi energy is shown as a vertical dashed−dotted line.

**Table 1. Predicted Defect Concentrations, Energy Barriers, Mobilities, and Electronic Conductivities at 300 K for the Most Prevalent Defects in MgS and $MgS_2$[a]**

| System | Defect | Formation energy (eV) | Concentration ($cm^{-3}$) | Migration barrier (eV) | Mobility ($cm^2\ V^{-1}\ s^{-1}$) | Conductivity ($S\ cm^{-1}$) |
|---|---|---|---|---|---|---|
| MgS | $V''_{Mg}$ | 1.28 | 9.79 | 1.42 | $1.38 \times 10^{-24}$ | $2.71 \times 10^{-23}$ |
| | $Mg_i^{\bullet\bullet}$ | 1.33 | 9.79 | 1.01 | $8.37 \times 10^{-18}$ | $1.64 \times 10^{-16}$ |
| $MgS_2$ | e′ | 1.83 | $3.48 \times 10^{-9}$ | 0.53 | $1.06 \times 10^{-9}$ | $3.69 \times 10^{-18}$ |
| | $V''_{Mg}$ | 2.17 | $6.65 \times 10^{-15}$ | 1.73 | $1.18 \times 10^{-29}$ | $1.58 \times 10^{-43}$ |

[a]The values in the table are derived from the defect formation energies of the S-rich region, which has a higher concentration of the prevalent defects.

e″ requires an initial structural distortion in which the bond distance of an S−S pair is increased. Note that the calculations with two extra electrons without any initial distortion result in the formation of two separate e′. The formation of e″ drives a significant increase in the S−S distance to ∼3.15 Å as illustrated in Figure 2c. The DOS plot shown in Figure S6 confirms the localization of e′ and e″ in $MgS_2$.

**Native Defects in MgS and $MgS_2$.** Figure 3 depicts the energy of formation of defects in MgS and $MgS_2$ as a function of Fermi energy. The formation energy is calculated using eq 1 where the chemical potentials, $\mu$, for Mg and S are defined for each region of the phase diagram in which the investigated material is in thermodynamic equilibrium. The chemical potential varies with the chemical environment of the system; i.e., the chemical nature of the reservoir defines the chemical potential that is qualitatively given as a Mg-rich region (S-poor region) or a Mg-poor region (S-rich region). The phases at thermodynamic equilibrium are determined using the data from the Open Quantum Materials Database (OQMD).[39]

In particular, the phases in thermodynamic equilibrium with MgS at 0 K are Mg (Mg-rich or reducing conditions) and $MgS_2$ (Mg-poor or oxidizing conditions). Likewise, $MgS_2$ is in thermodynamic equilibrium with MgS and S. Thus, the limiting values of chemical potential for calculating the defect formation energies in MgS are defined by the Mg−MgS (Mg-rich) and MgS−$MgS_2$ (Mg-poor) pseudobinaries. Similarly for $MgS_2$, the limiting chemical potential value is pinned by the MgS−$MgS_2$ (Mg-rich) and $MgS_2$−S (Mg-poor) regions.

Several types of defects such as magnesium vacancies ($V_{Mg}$), magnesium interstitials ($Mg_i$), sulfur vacancies ($V_S$), sulfur interstitials ($S_i$), hole polarons, and electron polarons with different charge states were considered. The Kröger−Vink notation is used hereafter to represent the defect types and their charge states. The charges of the defects are denoted in the superscript (e.g., • for positive, ′ for negative, and $x$ for neutral defects). Double symbols represent two positive or negative charges. The slope of each line in Figure 3 defines the charge state of that defect. In other words, a region of the curve with a positive (negative) slope represents a formation energy of positively (negatively) charged defects. In contrast, a neutral defect has a slope of zero (horizontal line).

The equilibrium Fermi level ($E_{Fermi}$) is determined using the charge neutrality condition ($\sum c_i q_i = 0$) and is shown as a vertical dashed−dotted line in Figure 3. Defects with low


https://doi.org/10.1021/acs.chemmater.2c03784
Chem. Mater. XXXX, XXX, XXX−XXX

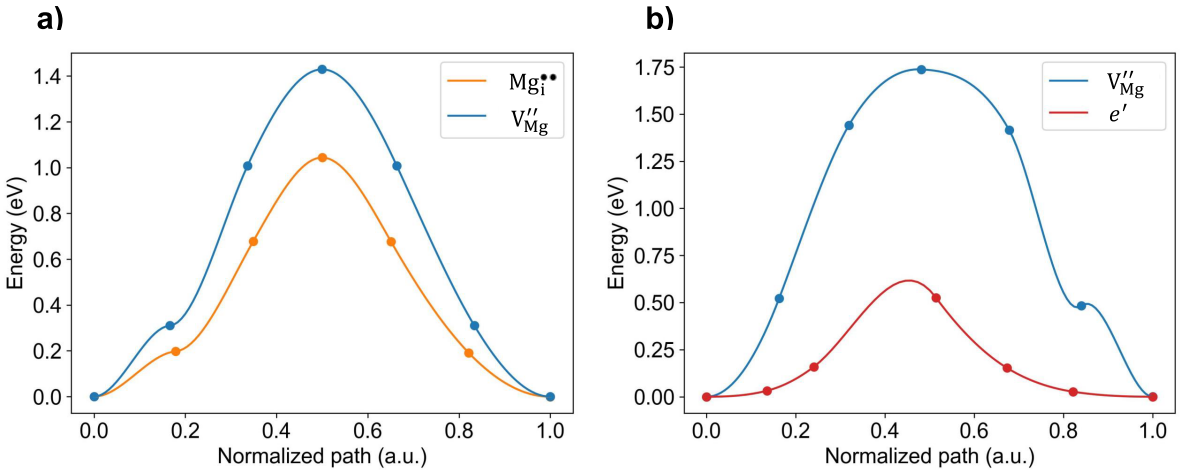


**Figure 4.** Energy barriers for the prevalent defects in (a) MgS and (b) $MgS_2$.

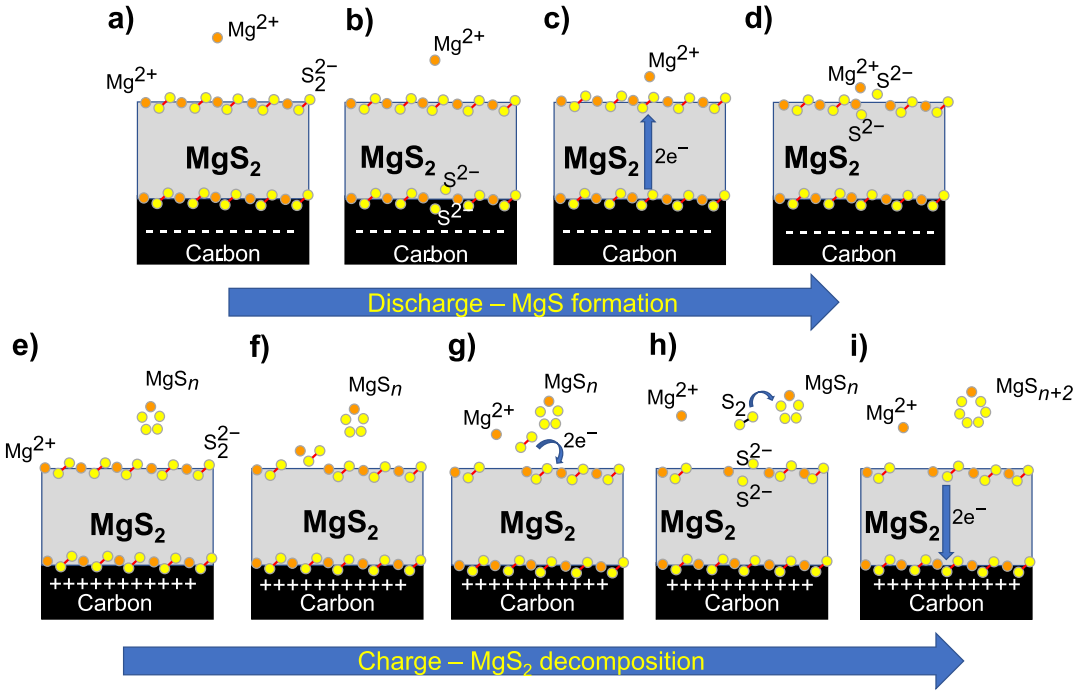


**Figure 5.** (a–d) MgS formation at the battery cathode during discharge after $MgS_2$ has been formed and (e–i) $MgS_2$ decomposition at the battery cathode during charge. The MgS formation during the discharge proceeds as follows. (a) $MgS_2$ immediately above the carbon accepts electrons from the external circuit, while $Mg^{2+}$ ions from the electrolyte approach the uppermost surfaces of $MgS_2$. (b) Two electrons from the carbon break a disulfide and form two $S^{2-}$ ions. (c) The electrons migrate toward the electrolyte–$MgS_2$ interface. (d) Two electrons arrive at the electrolyte–$MgS_2$ interface where a $Mg^{2+}$ ion is deposited. The $MgS_2$ decomposition during the charging process proceeds as follows. (e) $MgS_n$ polysulfides from the electrolyte approach the uppermost $MgS_2$. (f) A $Mg^{2+}$ ion from the $MgS_2$ surface moves toward the electrolyte due to the positive potential. A disulfide ion follows the moving $Mg^{2+}$ ion due to an electrostatic attraction. (g) The $Mg^{2+}$ ion is dissolved in the electrolyte, while the leaving disulfide ion donates two electrons to another disulfide ion at the electrolyte–$MgS_2$ interface. The leaving disulfide ion becomes a transient $S_2$ species, and the other disulfide ion at the interface breaks into two distinct $S^{2-}$ ions. (h) The transient $S_2$ ion joins the $MgS_n$ polysulfide forming a longer $MgS_{n+2}$ polysulfide. (i) The two electrons at the interface migrate toward the carbon electrode. Note that the electron migrations within $MgS_2$ in steps c and i are the same but in opposite directions.

formation energies at $E_{Fermi}$ are considered as the thermodynamically dominant defects. The concentrations of the two most prevalent defects at 300 K are listed in Table 1. The remaining defects are significantly less thermodynamically favourable and not considered further in this work. Note that the neutral defects are not taken into consideration as they do not contribute to either electron or hole transport.

Panels a and b of Figure 3 illustrate the formation energies of the defects in MgS for the Mg–MgS and MgS–$MgS_2$ regions, respectively. The defect with the lowest formation energy is $V_S^x$ for the MgS–$MgS_2$ region, but it is not considered for further analysis because the neutral defects do not contribute to charge transport. $V''_{Mg}$ and $Mg_i^{\bullet\bullet}$ are the most favorable charged defects with the lowest defect formation energies for the Mg-rich (reducing) and S-rich (oxidative) regions, resulting in a


https://doi.org/10.1021/acs.chemmater.2c03784
Chem. Mater. XXXX, XXX, XXX–XXX

high defect concentration of ~9.78 $cm^{-3}$. Note that we investigated three distinct interstitial positions for Mg and S in MgS, and only the Mg and S interstitial defects with the lowest formation energies are shown in panels a and b of Figure 3. The interstitial sites are searched and found using interstitial finding tool in the PYCDT package.

The defect formation energies for $MgS_2$ are shown for the MgS−$MgS_2$ and $MgS_2$−S regions in panels c and d of Figure 3, respectively. The neutral S vacancy, $V^x_S$, has the lowest formation energy for the Mg-rich (reducing) and S-rich (oxidative) regions, which do not make any contribution to charge transport. e′ is the most dominant charged defect in $MgS_2$ with a defect concentration of $3.4 \times 10^{-9}$ $cm^{-3}$. The second most prevalent defect is $V''_{Mg}$; it has a slightly higher defect formation energy compared to that of e′ but has a substantially lower concentration (~$6.6 \times 10^{-15}$ $cm^{-3}$). The interstitial defects in $MgS_2$ exhibit a very high formation energy with a defect formation energy of >3 eV.

**Mobility and Conductivity of Prevalent Defects in MgS and $MgS_2$.** The energy barriers associated with the migration of most prevalent defects in MgS and $MgS_2$ are calculated using the NEB method to gain deeper insight into their contribution to charge transport. Figure 4a depicts the minimum energy path (MEP) for the two most prevalent defects in MgS. The calculated mobility and conductivity values at 300 K are summarized in Table 1. $V''_{Mg}$ exhibits a very high migration barrier of 1.42 eV, which is consistent with a very high activation energy for ionic conduction reported on the basis of the experimental measurements.[14] Our migration barrier is higher than the previously reported value of ~0.9 eV obtained using a similar methodology and the PBE exchange-correlation functional.[17] The deviation can be most likely attributed to the use of different exchange-correlation functionals. In summary, the results of our study and Chen et al. show high values of migration barriers. The migration barrier of the other dominant charged defect, $Mg_i^{\bullet\bullet}$ is also characterized by a high migration barrier of ~1 eV. The mobilities of $V''_{Mg}$ and $Mg_i^{\bullet\bullet}$ calculated using eq 3 are $1.38 \times 10^{-24}$ and $8.35 \times 10^{-18}$ $cm^2\,V^{-1}\,s^{-1}$, respectively. Despite the predicted high concentrations of $V''_{Mg}$ and $Mg_i^{\bullet\bullet}$ defects, the estimated low mobility values originate from the high migration barriers. The low mobility, in turn leads to the poor conductivity values (see eq 4) of $Mg_i^{\bullet\bullet}$ and $V''_{Mg}$, which are computed to be ~$2.71 \times 10^{-23}$ and ~$1.64 \times 10^{-16}$ S $cm^{-1}$, respectively.

The MEP for the dominant defects in $MgS_2$ is shown in Figure 4b. Analogous to MgS, the $V''_{Mg}$ migration barrier in $MgS_2$ is also very high at ~1.73 eV. In contrast, e′ exhibits a relatively low diffusion barrier with the barrier height of ~0.53 eV. The relatively low energy barrier of e′ leads to a decent mobility at $1.06 \times 10^{-9}$ $cm^2\,V^{-1}\,s^{-1}$, which is several orders of magnitude higher than that of $V''_{Mg}$ ($1.18 \times 10^{-29}$ $cm^2\,V^{-1}\,s^{-1}$). However, due to the low concentration of e′, its estimated conductivity is negligible (~$3.69 \times 10^{-18}$ S $cm^{-1}$). Because of the high mobility of e′, its maximum diffusion lengths (i.e., the thickness of $MgS_2$ that can be traversed by the polaron) calculated using eq 5 are 3, 7, and 10 $\mu$m for discharge rates of 1, 0.2, and 0.1 C, respectively. This implies that the mobility of e′ is sufficient to traverse layers of $MgS_2$ and penetrate the cathode material, which is not the case for other defects in both MgS and $MgS_2$ due to their much lower mobility. Therefore, a way to improve the conductivity in $MgS_2$ is to enhance the concentration of e′, which can be achieved out of equilibrium at sufficiently high currents (>50 mA $cm^{-2}$).

**Polaron Kinetics in $MgS_2$.** So far, the analysis has been focused on the transport mechanism of the intrinsic defects formed under thermodynamic equilibrium conditions. However, the cathode material is not under equilibrium conditions during practical battery operations. Specifically, electrons from the external circuit and Mg ions from the electrolyte move into the cathode during discharge (Figure 5a−d). Conversely, electrons from $MgS_2$ move into the external circuit, $Mg^{2+}$ ions become dissolved in the electrolyte, and $S_2^{2-}$ ions merge with the polysulfide in the electrolyte during charge (Figure 5e−i). As shown in panels c and i of Figure 5, electron transport is clearly important in both scenarios.

We note that the electron transport mechanisms in panels c and i of Figure 5 are similar but occur in opposite directions. Notably, the electron transport during discharge is much easier to simulate than the transport during charge. The reason is that during discharge, the presence of an added $Mg^{2+}$ ion close to the electrolyte−$MgS_2$ interface acts as the driving force for electron migration, and the simulation supercell remains neutral. In contrast, the simulation of the charging process would require a charged supercell with a positive potential applied at the bottom of the $MgS_2$ model, which introduces a number of technical difficulties. Thus, we will focus on modeling the process of electron transport during discharge. Note that the transport during discharge is completely equivalent to that occurring during charge, except only for the direction of transport within the $MgS_2$ thin film. We analyzed electron transport during discharge by employing three distinct AIMD setups to comprehend the magnesiation process in $MgS_2$.

The migration of the $Mg^{2+}$ ion from the electrolyte into MgS is accompanied by two electrons coming from the external circuit during charge and maintains the charge neutrality of the system. The final goal is simulating a thin decomposition film of $MgS_2$ in which electrons come into the material from one side (that of the current collector), while $Mg^{2+}$ ions come from the side of the electrolyte. Subsequently, we study the mechanism of recombination of $Mg^{2+}$ and electrons in $MgS_2$. To gain a better understanding, we tackle the problem in three steps. (i) We run AIMD simulations of electron polarons in bulk $MgS_2$. (ii) We run an AIMD simulation of a $MgS_2$ thin film with an electron polaron added on one side of the film and a $Mg^{2+}$ ion on the other without explicitly including electrolyte molecules. (iii) We repeat step ii, but now including electrolyte molecules in the simulation.

In the first step, we determine whether the two electrons, required to neutralize a $Mg^{2+}$ ion can exist in the electrode bulk as either two separated e′ entities or as an e″. The computed defect formation energies suggest that the electrons used to neutralize an intercalating $Mg^{2+}$ organize more favorably as two separated e′ entities than a combined e″. However, the mechanism of $Mg^{2+}$ neutralization can differ significantly under non-equilibrium conditions that govern battery operation. In general, in regimes of thermodynamic equilibrium, the defect concentration is low, and thus, it is most likely that e′ will remain apart from each other avoiding the formation of e″. However, in a realistic scenario, under non-equilibrium conditions, the concentration of the e′ can be high enough for them to lie closer. On the basis of these considerations, our first AIMD model simulates the evolution of two nearby e′ in the bulk of $MgS_2$, which is modeled using a 2 × 2 × 2 supercell


https://doi.org/10.1021/acs.chemmater.2c03784
Chem. Mater. XXXX, XXX, XXX−XXX

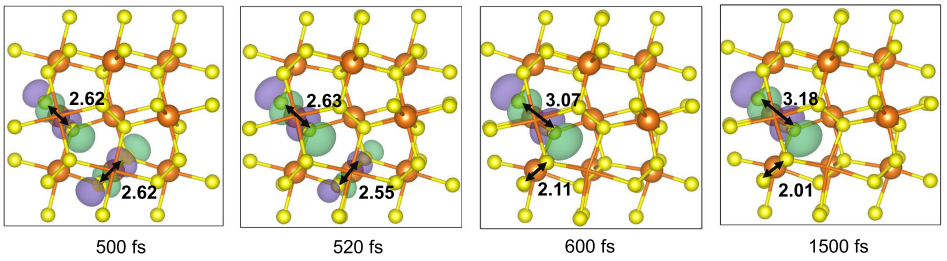


**Figure 6.** Snapshots of AIMD simulation for bulk $MgS_2$ with electron polarons at 350 K. The isosurface indicates the occupied $\sigma^*$ orbital.

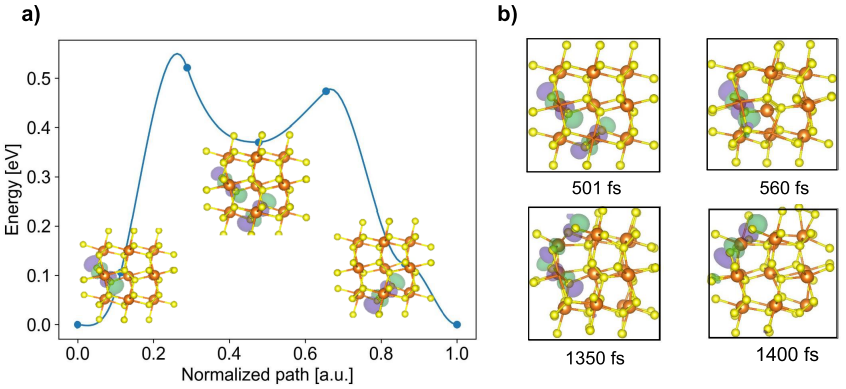


**Figure 7.** (a) Minimum energy path for e″ migration in $MgS_2$. (b) Snapshots of MD simulation of the $MgS_2$ bulk at 1000 K highlighting the localization of the point defects as they migrate in $MgS_2$. The isosurface indicates the occupied $\sigma^*$ orbital.

of the conventional unit cell with 96 atoms. The system is equilibrated for 500 fs, while two e′ entities are localized at two S dimers in the bulk crystal structure (the atomic coordinates of the S dimers with e′ are kept fixed during equilibration).

Snapshots of the AIMD simulation after equilibration are shown in Figure 6. Upon equilibration, it is clear that the electrons remain as two separate e′ entities. The e′ induces the structural distortion, as seen in the MD snapshots at 500 fs, where the S dimers with the e′ have an S−S bond distance of 2.62 Å. In subsequent MD runs, the two e′ entities merge to form e″ and localize on one S dimer; i.e., we observe a single dimer completely broken, with the two sulfur ions separated by 3.1 Å, while the other dimer completely recovers its disulfide nature (the S−S distance is restored to 2.1 Å). After the two e′ entities merge, we do not observe further migration of e″ in the AIMD simulations.

As no migration of e″ is observed, we performed a NEB calculation to assess its migration characteristics. The migration of e″ from one site to an adjacent (but equivalent) site happens via an intermediate step at which e″ splits into two e′ entities, as shown in Figure 7a. The initial and final images of the NEB have e″ localized in one S dimer, while this dimer splits into two distinct e′ entities in the middle image. The energy barrier for the formation of two e′ entities from e″ is estimated to be as high as ∼0.52 eV. This high activation energy is consistent with the fact that the migration of e″ is also not observed in our MD simulation at 350 K.

To provide further insight into the kinetics of defect recombination, we performed a subsequent AIMD simulation at a high temperature (1000 K), where it is expected to observe a migration event for an ∼0.52 eV barrier. Note that the simulation is performed at a higher temperature to accelerate the occurrence of rare events. The snapshots of the AIMD simulation are shown in Figure 7b. The two e′ entities combine to form e″ during the initial steps of the MD simulation, which is similar to the MD simulation results at 350 K. However, the e″ starts to diffuse into the lattice by splitting into two e′ entities, in agreement with our NEB calculation results. Consequently, we conclude that the electrons from the external circuit migrate through the electrode in the form of e″.

Now we can answer the question posed in the introduction about the charge transport mechanism in $MgS_2$ that enables the formation of MgS. Because the migration barrier for e″ in $MgS_2$ is virtually the same as that of e′, we can conclude that their maximum diffusion length will also be similar. Thus, at a rate of 1 C, $MgS_2$ thin films up to 3 $\mu$m thick may be formed on the cathode, and e″ will be able to reach the film surface in contact with the electrolyte, where they will recombine with $Mg^{2+}$ ions, starting to nucleate MgS.

From the AIMD simulations in the bulk, we can anticipate that, for sufficiently high currents (>50 mA $cm^{-2}$), the electrons coming from the current collector will initially combine to form e″ in a $MgS_2$ film, before they migrate toward $Mg^{2+}$ species within the material. Under this assumption, we built a second MD model slab of a (001) $MgS_2$ surface to study the magnesiation process in $MgS_2$. In this model, a slab thickness of ∼18 Å is separated from its replicas by ∼16 Å of vacuum. The system is subsequently equilibrated for 500 fs with the e″ localized on one of the S−S bonds located near one side of the slab, while we place a Mg (metallic) atom on the opposite side of the slab model. Note that during the AIMD equilibration, the atomic coordinates of the Mg atom and the S atoms with the e″ localized are kept fixed. A dipole correction (average correction of ∼−1.87 D) is applied in the direction of the surface to compensate for the dipole moment that arises from the asymmetry along the nonperiodic ($z$) direction.


https://doi.org/10.1021/acs.chemmater.2c03784
Chem. Mater. XXXX, XXX, XXX−XXX

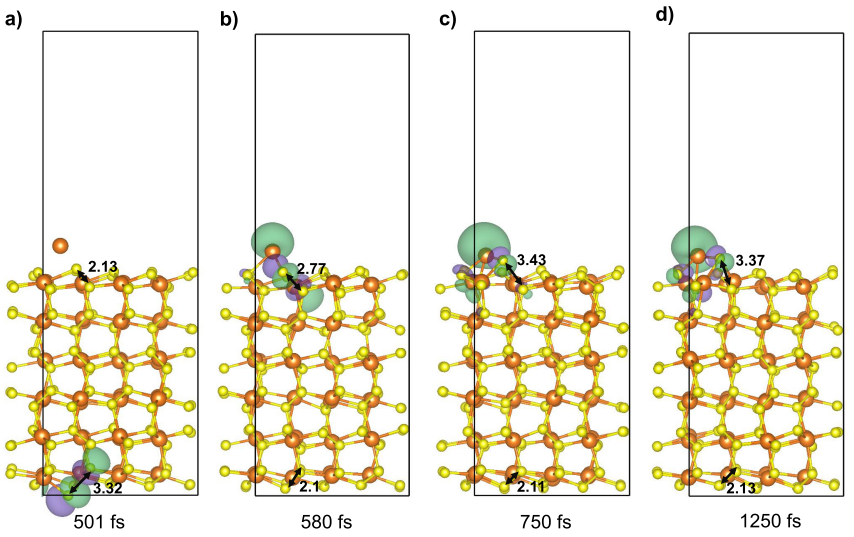


**Figure 8.** Snapshots of AIMD simulation with Mg at the (001) surface of $MgS_2$ at 350 K. The isosurface indicates the occupied $\sigma^*$ orbital.

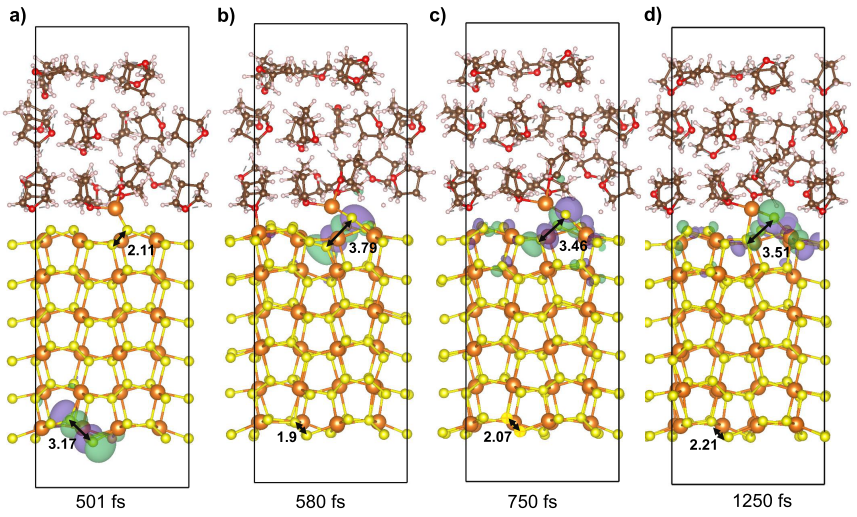


**Figure 9.** Snapshots of AIMD at the (001) surface of $MgS_2$ in contact with a THF solvent (top) and a boron nitride sheet (bottom) at 350 K. The isosurface indicates the occupied $\sigma^*$ orbital.

Figure 8 depicts snapshots taken from the AIMD simulations. During the AIMD equilibration, one can see that the e″ is effectively localized at the bottom of the slab model, which quickly is transferred to the top surface as the $Mg^{2+}$ approaches the $MgS_2$ surface from the opposite side. The process of charge transfer is directly reflected by a decrease in the interatomic distance of the S dimer, in which the charge was originally localized. The S−S distance of the S dimer at which the polaron is localized at the beginning of the AIMD simulation decreased from ∼3.32 to ∼2.13 Å. In contrast, the interaction with $Mg^{2+}$ elongated the S−S distance (of the S dimer) at the surface from ∼2.13 to ∼3.37 Å. An increase in the S−S distance upon the interaction with $Mg^{2+}$ can be understood as the formation of MgS at the surface. From a closer inspection of our AIMD simulations, we could not detect any gradual charge transport; indeed, the localized charge at the bottom of the slab abruptly shifts toward the top surface when $Mg^{2+}$ begins the approach with the $MgS_2$ surface. This scenario resembles an electron tunneling mechanism, but it is not. Electron tunneling cannot be modeled in AIMD simulations because this computational framework is completely adiabatic (i.e., for each nuclear arrangement, the electrons are in their ground state, without considering the electron density of the previous time step). Indeed, it is an artifact of our model approach. The electric field created by the added $Mg^{2+}$ ion on the top surface makes it more favorable to localize electrons in a disulfide unit close to it than in the dissociated disulfide that we enforced on the bottom surface. To study the non-adiabatic effect, we should use Ehrenfest dynamics, which is prohibitively expensive considering the size of the supercell used in this study.

We carried out additional AIMD simulations. In particular, we build a model in which the liquid electrolyte is considered explicitly. We expected that the addition of the solvent molecules could screen the strong electric field created by the added $Mg^{2+}$ ion and thus allow us to observe the diffusion of polarons through the thin film. In practice, in these new AIMD simulations, we filled the ∼16 Å of vacuum with tetrahydrofuran (THF) molecules, a commonly used electrolyte solvent in magnesium batteries. Using GROMACS,[40] 18 THF molecules are added to match the experimental density of ∼0.88 g $cm^{-3}$ at ∼298 K.[41] In addition, a layer of a wide-gap


https://doi.org/10.1021/acs.chemmater.2c03784
Chem. Mater. XXXX, XXX, XXX−XXX

semiconductor, boron nitride (BN), is introduced on the opposite side of the slab model to prevent the leakage of charge from the lower surface of the slab into the electrolyte. Following the preliminary relaxation at 0 K, the electrolyte is further equilibrated at 350 K for 0.5 ps while keeping the rest of the system (slab and boron nitride layer) frozen. Subsequently, every atom in the system except the BN layer is equilibrated for 1 ps to establish the interaction between the cathode and the electrolyte. Figure 9 shows snapshots of the AIMD run.

Notably, we observed a similar process of magnesiation as seen in the AIMD simulations, but in the absence of an electrolyte. These findings suggest that effects associated with electrolyte screening are still unable to prevent the artificial abrupt shift of the electron toward the electrolyte−$MgS_2$ interface.

## CONCLUSION

In summary, using first-principles calculations and *ab initio* molecular dynamics, we studied the two experimentally observed solid discharge products in Mg−sulfur battery cathodes, i.e. MgS and $MgS_2$. We unveiled that $MgS_2$ can hold electronic conduction through a mechanism entailing the migration of double electron polaron species. Despite the very low concentration of electron polarons in thermodynamic equilibrium in $MgS_2$, the non-equilibrium conditions during battery operation (typically at a discharge rate of 1 C) and the relative fast polaron migration (migration barriers around 0.5 eV) enable the electronic conduction up to 3 $\mu$m in $MgS_2$ deposits.

During discharge, the polaron electronic conduction in $MgS_2$ allows the redox process to progress to the formation of MgS. However, we observe that a very slow migration of charged defects and/or polarons in MgS curbs the redox process and severely hinders the cyclability of the battery. Contrary to previous reports ascribing the poor cyclability of Mg−sulfur batteries to the formation of both $MgS_2$ and MgS,[13] we demonstrate the importance of preventing the further oxidation of $MgS_2$ to MgS. These findings encourage the design of experimental strategies that include the oxidation of $MgS_2$.

## ASSOCIATED CONTENT

### Supporting Information

The Supporting Information is available free of charge at https://pubs.acs.org/doi/10.1021/acs.chemmater.2c03784.

Crystal structures of MgS and $MgS_2$, calibration of $\alpha$ for the HSE functional, band structures of MgS and $MgS_2$, occupation of frontier orbitals in sulfides and disulfides, and DOS plots for polaron structures in MgS and $MgS_2$ (PDF)

## AUTHOR INFORMATION


### Corresponding Authors

**Pieremanuele Canepa** − *Department of Materials Science and Engineering, National University of Singapore, Singapore 117575; Department Chemical and Biomolecular Engineering, National University of Singapore, Singapore 117585;* orcid.org/0000-0002-5168-9253; Email: pcanepa@nus.edu.sg

**Juan Maria García-Lastra** − *Department of Energy Conversion and Storage, Technical University of Denmark, Kongens Lyngby 2800, Denmark;* orcid.org/0000-0001-5311-3656; Email: jmgla@dtu.dk

### Authors

**Smobin Vincent** − *Department of Energy Conversion and Storage, Technical University of Denmark, Kongens Lyngby 2800, Denmark;* orcid.org/0000-0002-6147-4360

**Jin Hyun Chang** − *Department of Energy Conversion and Storage, Technical University of Denmark, Kongens Lyngby 2800, Denmark;* orcid.org/0000-0003-0668-4530

Complete contact information is available at: https://pubs.acs.org/10.1021/acs.chemmater.2c03784


### Notes

The authors declare no competing financial interest.

## ACKNOWLEDGMENTS

The authors thank Piotr Jankowski for fruitful discussions. The authors acknowledge support from the "European Magnesium Interactive Battery Community (e-Magic)" FET-Proactive project (Contract 824066). P.C. acknowledges funding from the National Research Foundation (NRF) under NRF Fellowship NRFF12-2020-0012.

## REFERENCES


(1) Bieker, G.; KüPers, V.; Kolek, M.; Winter, M. Intrinsic Differences and Realistic Perspectives of Lithium-Sulfur and Magnesium-Sulfur Batteries. *Commun. Mater.* **2021**, *2*, 37.

(2) Chung, S.-H.; Manthiram, A. Current Status and Future Prospects of Metal-Sulfur Batteries. *Adv. Mater.* **2019**, *31*, 1901125.

(3) Durmus, Y. E.; Zhang, H.; Baakes, F.; Desmaizieres, G.; Hayun, H.; Yang, L.; Kolek, M.; KüPers, V.; Janek, J.; Mandler, D.; et al. Side by Side Battery Technologies with Lithium-Ion Based Batteries. *Adv. Energy Mater.* **2020**, *10*, 2000089.

(4) Hong, X.; Mei, J.; Wen, L.; Tong, Y.; Vasileff, A. J.; Wang, L.; Liang, J.; Sun, Z.; Dou, S. X. Nonlithium Metal−Sulfur Batteries: Steps Toward a Leap. *Advanced materials* **2019**, *31*, 1802822.

(5) Zu, C.-X.; Li, H. Thermodynamic Analysis on Energy Densities of Batteries. *Energy Environ. Sci.* **2011**, *4*, 2614−2624.

(6) Schmuch, R.; Wagner, R.; Hörpel, G.; Placke, T.; Winter, M. Performance and Cost of Materials for Lithium-Based Rechargeable Automotive Batteries. *Nature Energy* **2018**, *3*, 267−278.

(7) Hans Wedepohl, K. The composition of the continental crust. *Geochim. Cosmochim. Acta* **1995**, *59*, 1217−1232.

(8) Aurbach, D.; Lu, Z.; Schechter, A.; Gofer, Y.; Gizbar, H.; Turgeman, R.; Cohen, Y.; Moshkovich, M.; Levi, E. Prototype Systems for Rechargeable Magnesium Batteries. *Nature* **2000**, *407*, 724−727.

(9) Shterenberg, I.; Salama, M.; Yoo, H. D.; Gofer, Y.; Park, J.-B.; Sun, Y.-K.; Aurbach, D. Evaluation of (CF3SO2) 2N-(TFSI) Based Electrolyte Solutions for Mg Batteries. *J. Electrochem. Soc.* **2015**, *162*, A7118.

(10) Zhao-Karger, Z.; Zhao, X.; Wang, D.; Diemant, T.; Behm, R. J.; Fichtner, M. Performance Improvement of Magnesium Sulfur Batteries with Modified Non-Nucleophilic Electrolytes. *Adv. Energy Mater.* **2015**, *5*, 1401155.

(11) Zhao, X.; Yang, Y.; NuLi, Y.; Li, D.; Wang, Y.; Xiang, X. A New Class of Electrolytes Based on Magnesium Bis(Diisopropyl)Amide for Magnesium−Sulfur Batteries. *Chem. Commun.* **2019**, *55*, 6086−6089.

(12) Gao, T.; Ji, X.; Hou, S.; Fan, X.; Li, X.; Yang, C.; Han, F.; Wang, F.; Jiang, J.; Xu, K.; et al. Thermodynamics and Kinetics of Sulfur Cathode during Discharge in MgTFSI2−DME Electrolyte. *Adv. Mater.* **2018**, *30*, 1704313.

(13) Häcker, J.; Danner, C.; Sievert, B.; Biswas, I.; Zhao-Karger, Z.; Wagner, N.; Friedrich, K. A. Investigation of Magnesium−Sulfur

Batteries Using Electrochemical Impedance Spectroscopy. *Electrochim. Acta* **2020**, *338*, 135787.
(14) Nakamura, H.; Ogawa, Y.; Kasahara, A.; et al. Ionic and Positive Hole Conductivities of Solid Magnesium and Strontium Sulfides. *Transactions of the Japan institute of metals* **1984**, *25*, 692−697.
(15) Nakamura, H.; Ogawa, Y.; Kasahara, A.; Iwasaki, S. Sulfur Pressure Dependence of Electrical Conductivity of Group IIa and IIIa Metal Sulfides. *Mater. Trans., JIM* **1995**, *36*, 1263−1270.
(16) Puntambekar, U.; Veliah, S.; Pandey, R. Point-Defects in Magnesium Sulfide. *Journal of materials research* **1994**, *9*, 132−134.
(17) Chen, T.; Sai Gautam, G.; Canepa, P. Ionic Transport in Potential Coating Materials for Mg Batteries. *Chem. Mater.* **2019**, *31*, 8087−8099.
(18) Kresse, G.; Furthmüller, J. Efficiency of Ab-Initio Total Energy Calculations for Metals and Semiconductors Using a Plane-Wave Basis Set. *Comput. Mater. Sci.* **1996**, *6*, 15−50.
(19) Kresse, G.; Furthmüller, J. Efficient Iterative Schemes for *ab initio* Total-Energy Calculations Using a Plane-Wave Basis Set. *Phys. Rev. B* **1996**, *54*, 11169−11186.
(20) Perdew, J. P.; Burke, K.; Ernzerhof, M. Generalized Gradient Approximation Made Simple. *Phys. Rev. Lett.* **1996**, *77*, 3865−3868.
(21) Haastrup, S.; Strange, M.; Pandey, M.; Deilmann, T.; Schmidt, P. S.; Hinsche, N. F.; Gjerding, M. N.; Torelli, D.; Larsen, P. M.; Riis-Jensen, A. C.; et al. The Computational 2D Materials Database: High-Throughput Modeling and Discovery of Atomically Thin Crystals. *2D Materials* **2018**, *5*, 042002.
(22) Heyd, J.; Scuseria, G. E.; Ernzerhof, M. Hybrid Functionals Based on a Screened Coulomb Potential. *J. Chem. Phys.* **2003**, *118*, 8207−8215.
(23) Krukau, A. V.; Vydrov, O. A.; Izmaylov, A. F.; Scuseria, G. E. Influence of the Exchange Screening Parameter on the Performance of Screened Hybrid Functionals. *J. Chem. Phys.* **2006**, *125*, 224106.
(24) Hedin, L. New Method for Calculating the One-Particle Green's Function with Application to the Electron-Gas Problem. *Phys. Rev.* **1965**, *139*, A796.
(25) Hybertsen, M. S.; Louie, S. G. Electron Correlation in Semiconductors and Insulators: Band Gaps and Quasiparticle Energies. *Phys. Rev. B* **1986**, *34*, 5390.
(26) Shishkin, M.; Kresse, G. Self-Consistent G W Calculations for Semiconductors and Insulators. *Phys. Rev. B* **2007**, *75*, 235102.
(27) Blöchl, P. Projector Augmented-Wave Method. *Phys. Rev. B* **1994**, *50*, 17953−17979.
(28) Ganose, A. M.; Jackson, A. J.; Scanlon, D. O. Sumo: Command-Line Tools for Plotting and Analysis of Periodic Ab Initio Calculations. *Journal of Open Source Software* **2018**, *3*, 717.
(29) Freysoldt, C.; Neugebauer, J.; Van de Walle, C. G. Fully Ab Initio Finite-Size Corrections for Charged-Defect Supercell Calculations. *Physical review letters* **2009**, *102*, 016402.
(30) Broberg, D.; Medasani, B.; Zimmermann, N. E.; Yu, G.; Canning, A.; Haranczyk, M.; Asta, M.; Hautier, G. PyCDT: A Python Toolkit for Modeling Point Defects in Semiconductors and Insulators. *Comput. Phys. Commun.* **2018**, *226*, 165−179.
(31) Tilley, R. J. *Defects in Solids*; John Wiley & Sons, 2008.
(32) Henkelman, G.; Jónsson, H. Improved Tangent Estimate in the Nudged Elastic Band Method for Finding Minimum Energy Paths and Saddle Points. *J. Chem. Phys.* **2000**, *113*, 9978−9985.
(33) Hjorth Larsen, A.; Jørgen Mortensen, J.; Blomqvist, J.; Castelli, I. E.; Christensen, R.; Dułak, M.; Friis, J.; Groves, M. N.; Hammer, B.; Hargus, C.; et al. The Atomic Simulation Environment−a Python Library for Working with Atoms. *J. Phys.: Condens. Matter* **2017**, *29*, 273002.
(34) Mali, G. *Ab initio* Crystal Structure Prediction of Magnesium (Poly)Sulfides and Calculation of Their NMR Parameters. *Acta Crystallographica Section C: Structural Chemistry* **2017**, *73*, 229−233.
(35) Primak, W.; Kaufman, H.; Ward, R. X-Ray Diffraction Studies of Systems Involved in the Preparation of Alkaline Earth Sulfide and Selenide Phosphors [1]. *J. Am. Chem. Soc.* **1948**, *70*, 2043−2046.
(36) Lany, S. Polymorphism, Band-Structure, Band-Lineup, and Alloy Energetics of the Group II Oxides and Sulfides MgO, ZnO, CdO, MgS, ZnS, CdS. Oxide-based Materials and Devices V. 2014; pp 109−116.
(37) Zhao, C.; Duan, Y.; Gao, J.; Dong, H. Crystal and Band Structures of ZnS, MgS, and ZnS-MgS Alloys. *J. Appl. Phys.* **2017**, *121*, 235705.
(38) Smith, J. G.; Naruse, J.; Hiramatsu, H.; Siegel, D. J. Intrinsic Conductivity in Magnesium-Oxygen Battery Discharge Products: MgO and MgO2. *Chem. Mater.* **2017**, *29*, 3152−3163.
(39) Saal, J. E.; Kirklin, S.; Aykol, M.; Meredig, B.; Wolverton, C. Materials Design and Discovery with High-Throughput Density Functional Theory: The Open Quantum Materials Database (OQMD). *Jom* **2013**, *65*, 1501−1509.
(40) Abraham, M. J.; Murtola, T.; Schulz, R.; Páll, S.; Smith, J. C.; Hess, B.; Lindahl, E. GROMACS: High Performance Molecular Simulations through Multi-Level Parallelism from Laptops to Supercomputers. *SoftwareX* **2015**, *1*, 19−25.
(41) Guard, U. C. *Chemical Hazard Response Information System (CHRIS)-Hazardous Chemical Data*; Commandant Instruction, 1999; p 16465.


https://doi.org/10.1021/acs.chemmater.2c03784
*Chem. Mater.* XXXX, XXX, XXX−XXX